



Electric field-induced crossover from 3D to 2D topological defects in a nematic liquid crystal: Experimental verification

Journal:	<i>Soft Matter</i>
Manuscript ID	SM-ART-08-2019-001733.R2
Article Type:	Paper
Date Submitted by the Author:	29-Oct-2019
Complete List of Authors:	Ferris, Andrew; Case Western Reserve University, Physics Afghah, Sajedah; Kent State University, Liquid Crystal Institute Selinger, Jonathan; Kent State University, Liquid Crystal Institute Selinger, Robin; Kent State University, Liquid Crystal Institute Rosenblatt, Charles; Case Western Reserve University, Dept. of Physics

ARTICLE

Electric field-induced crossover from 3D to 2D topological defects in a nematic liquid crystal: Experimental verification

Andrew J. Ferris^a, Sajedeh Afghah^b, Robin L.B. Selinger^b, Jonathan V. Selinger^b, and Charles Rosenblatt^{a,†}

Received 00th January 20xx,
Accepted 00th January 20xx

DOI: 10.1039/x0xx00000x

A substrate was patterned with two pairs of half-integer strength topological defects, $(+\frac{1}{2}, +\frac{1}{2})$ and $(+\frac{1}{2}, -\frac{1}{2})$. In a sufficiently thick cell, a disclination line runs in an arch above the substrate connecting the two half integer defects within each pair. The director around the disclination line for the like-sign pair must rotate in 3D, whereas for the opposite-sign defect pair the director lies in the xy -plane parallel to the substrate. For a negative dielectric anisotropy nematic, an electric field applied normal to the substrate drives the director into the xy -plane, forcing the arch of the disclination line of the like-sign pair to become extended along the z -axis. For sufficiently large field the arch splits, resulting in two nearly parallel disclination lines traversing the cell from one substrate to the other. The opposite-sign defect pair is largely unaffected by the electric field as the director already lies in the xy -plane. Experimental results are presented, which are consistent with numerical simulations.

1 Introduction

Topological defects (TDs) are pervasive throughout nature^{1,2}, and are fundamental to central questions in science and technology³⁻⁵. Owing to their large optical, electrical, and magnetic anisotropies, liquid crystals (LCs) can serve as an ideal test bed for visualizing TDs^{6,7,8}; understanding their structure, energetics, and dynamics; and novel applications requiring path-specific transport of electrical charge or material.

Topological defects in liquid crystals can take many forms, including so-called “oily”⁹ and “soapy streaks”¹⁰, twist grain boundary^{11,12}, and parabolic focal conic¹³ defects in the smectic phases, as well as simple point, line, and surface defects in the nematic phase⁶. Here we focus on point and line defects, in particular point defects at a surface at which the director orientation is ill-defined and the “disclination line” defects that emanate from the surface. As one circumnavigates the surface point defect, the defect strength m is defined as the number of rotations made by the director, which can assume any half-integer or integer value. The fundamental defect strength is $m_0 = \pm\frac{1}{2}$; one (of several) pathways by which any higher strength defect can relax its elastic energy cost is by splitting into a pair (or pairs) of defects of strength m_0 . For a liquid crystal residing in three dimensional space, the defect extends from the surface as a line disclination and terminates either at another location on the same surface or on the opposing substrate^{14,15}. The properties of these disclinations as functions of electric field,

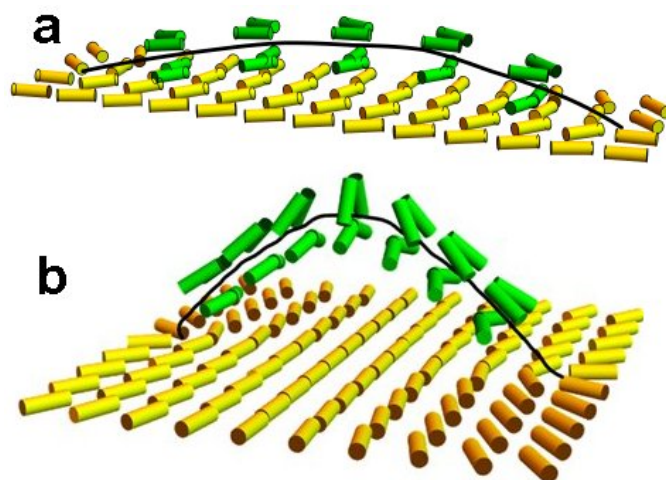


Fig. 1 Numerical simulations showing director patterns at surfaces and disclination arches that connect the two half-integer defects. a) opposite-sign defect pair of strength $(+\frac{1}{2}, -\frac{1}{2})$, in which the director field is quasi-2D along the entire disclination line. b) same-sign defect pair of strength $(+\frac{1}{2}, +\frac{1}{2})$, but with a 3D director field along the disclination line. Notice that in the absence of an electric field, the ratio between the disclination arch height and surface defect spacing is about 0.08 and 0.36 for Figs. 1a and 1b, respectively. We remark that the region shown in Fig. 1a is taken from a larger simulation, which includes two separate defect pairs, both $(+1/2, -1/2)$. Here reflection symmetry is broken because of the interaction of this defect pair with the other defect pair, outside the field of view. This asymmetry is not relevant to the current study, because a defect pair is not required to have a reflection symmetry.

surface anchoring, and cell thickness have drawn recent attention¹⁶.

Crucial to their behaviour is dimensionality. Whereas previous work has emphasized differences between two-dimensions (2D) and three-dimensions (3D)^{6,17}, the theoretical work of Afghah¹⁶ and the experimental and numerical work

^a Dept. of Physics, Case Western Reserve University, Cleveland, Ohio 44106 USA

^b Dept. of Physics, Advanced Materials and Liquid Crystal Institute, Kent State University, Kent, Ohio 44242 USA

[†] Author for correspondence. Email address: rosenblatt@case.edu

presented herein focus on the *crossover* from 3D to 2D in the presence of an electric field.

If the nematic director is confined to the 2D *xy*-plane, as occurs at a surface point defect with planar director anchoring, the strength m of the director disclination *line* can assume any half-integer or integer value. On the other hand, if the director is free to orient in 3D, all half-integer disclinations can be transformed smoothly from one into another and therefore are topologically equivalent. Thus, there are infinitely many strengths ($m = \pm\frac{1}{2}, \pm 1, \pm\frac{3}{2}, \text{etc.}$) of 2D disclinations, but only one unique half-integer defect strength in 3D, which is topologically equivalent to all other half-integer disclinations.

This distinction between 2D and 3D director fields is critical to the behaviour of liquid crystalline defects. Consider two sets of TDs located on a single surface, *viz.*, two closely-spaced (opposite-sign) $m = \pm\frac{1}{2}$ TDs and a closely-spaced (same-sign) $m = +\frac{1}{2}$ pair. Figures 1a ($m = \pm\frac{1}{2}$) and 1b ($m = +\frac{1}{2}$) show numerical simulations for these defect configurations. With appropriate boundary conditions, a half-integer strength bulk disclination line connects each pair of surface defects by matching the director orientation at the termination points. Consider the same-sign $m = +\frac{1}{2}$ pair of surface defects (Fig. 1b). The lowest energy half-integer strength configuration for the bulk disclination is one in which the director adopts an $m = -1/2$ configuration about the disclination at the apex. The director is oriented vertically at the peak of this apex, whereas it is oriented in the plane at the termination points corresponding to the two surface defects; thus the resulting director field is three-dimensional. Next consider the opposite-sign $m = \pm\frac{1}{2}$ surface defects (Fig. 1a). Energy minimization produces a director profile in which the director remains approximately parallel to the surface, *i.e.*, in the *xy*-plane, at all points around the disclination arch, as this facilitates the smooth transition from a half integer defect of one sign to that of the other sign. This corresponds to a two-dimensional director field around the disclination.

Afghah, et al. simulated this behaviour numerically¹⁶ using a negative dielectric anisotropy $\Delta\epsilon$ liquid crystal in an electric field applied normal to the surface. In such a field the director tends to align in a plane perpendicular to that field, *i.e.*, parallel to the surface. For sufficiently large electric field the director profile becomes quasi-2D, resulting in an elastic energy cost for the heretofore 3D-type disclination between the $m = +\frac{1}{2}$ surface defect pair. In order to accommodate this director profile, the disclination arch connecting the $m = +\frac{1}{2}$ surface defect pair becomes extended along the *z*-axis. For sufficiently large electric field the arch separates into a pair of disclination lines terminating in surface disclinations at the opposing open surface. In contrast, the disclination for the opposite-sign $m = \pm\frac{1}{2}$ pair is unaffected, as the director field around the arched disclination line already is two dimensional. Thus, the electric field-induced crossover from 3D to 2D director field behaviour forces the expulsion of disclination lines connecting certain types of surface defects that cannot be accommodated by a 2D director field disclination. On the other hand, other types of surface defects (opposite-sign $m = \pm\frac{1}{2}$ defects) can remain

connected by disclination lines that possess an inherently 2D director field.

In this paper we report on an experimental realization motivated by the numerical simulations in Ref. 16, in which our experiment is modified to correspond to physically realistic boundary conditions. We also include modelling results that utilize our experimental conditions. Experimentally, there are several techniques to create defects at a surface and their associated disclination lines^{15,18-24}, as well as to manipulate these defect lines in 3D^{15,25-35}. Here we exploit techniques developed in our laboratory^{15,35}, scribing two pairs of half-integer defect patterns (same-sign and opposite-sign) on a polymer-coated substrate, and impose uniform vertical (*i.e.*, homeotropic) alignment of the director at the opposing substrate. Both polarizing optical microscopy and fluorescent confocal polarizing microscopy show that an electric field applied normal to the substrates has no substantial effect on the disclination line that connects opposite-sign $m = \pm\frac{1}{2}$ surface TDs. On the other hand, the field distorts and eventually breaks the disclination line connecting the same sign $m = +\frac{1}{2}$ TDs, resulting in a pair of disclination lines running from one substrate to the other. Numerical simulations accounting for the experimentally required boundary conditions are presented, with results qualitatively similar to those of Ref. 16 in which open boundary conditions, *i.e.*, no preferred orientation, were examined. Our results demonstrate that half-integer disclination lines associated with 3D director fields (of which 2D director fields are a subset) can connect any either same-sign or opposite-sign half-integer surface defects. But when the bulk director field is quenched into a quasi-2D configuration, the available disclinations can be prevented on topological grounds from connecting certain pairs of surface defects.

2 Experimental Methods

Cells were constructed using a pair of semi-transparent indium-tin-oxide (ITO) coated glass slides as electrodes. One ITO-covered slide was spin-coated with the polyimide polyvinyl alcohol ($M_w = 31000 - 50000$) and baked at 120°C for 120 min. The polyimide was subsequently scribed by an atomic force microscope stylus with a pair of $m = +\frac{1}{2}$ defects whose cores were spaced $d = 12 \mu\text{m}$ apart along the *x*-axis using the technique described in Ref. 10. Another pair of defects having opposite-sign of strength $m = \pm\frac{1}{2}$ was scribed on the same substrate, approximately 300 μm from the same-sign defect pair. The opposing substrate consisted of a microscope slide coated with ITO and the polyimide SE-1211 (Nissan Chemical Industries), which was baked according to the manufacturer's specifications; this served as a substrate for vertical alignment of the director. We utilize an opposing "hard" substrate, one that also imposes vertical (homeotropic) alignment while facilitating application of an electric field. (Note that true "open" boundary conditions in Ref. 16 are not accessible experimentally.) Vertical alignment was chosen because, for planar degenerate anchoring at the opposing substrate, the arched disclination lines from the $m = +\frac{1}{2}$ pair always extended

to $m = -\frac{1}{2}$ defects outside the patterned region; energy calculations in Ref. 16 supported this observation.

The slides were then placed together, separated by Mylar spacers, and cemented. The thickness h was approximately 25 μm , as determined by the confocal microscope measurements. Since $h > 2d$ the disclination lines are expected to run between TDs on the same surface, rather than from one surface to the opposing surface^{14,35}.

We used the negative dielectric anisotropy mixture liquid crystal ZLI-2806 (Merck), which has a room temperature nematic phase. Its dielectric anisotropy $\Delta\epsilon = -4.8$ (Ref. 36) and its optical birefringence $\Delta n = 0.044$ (Ref. 37, supplemental information), both measured at room temperature. The relatively small birefringence ensured good depth resolution in our confocal fluorescent imaging experiments³⁸ (see below). Added to the liquid crystal was 0.005 wt-% of anisotropic fluorescent dye N,N-bis(2,5-di-tert-butylphenyl)-3,3',9,10'-perylene dicarboximide ("BTBP", Sigma-Aldrich).

The cell was filled with the LC/dye mixture in the isotropic phase by capillary action, and brought down to room temperature. First, polarizing optical microscope (POM) images were collected, with the sample residing between a pair of crossed polarizers. Here the intensity is given by $I = \frac{1}{2} I_0 \sin^2 2\varphi (1 - \cos\alpha)$, where α is the optical retardation corresponding to the integral through the sample thickness of the effective birefringence divided by the wavelength of light³⁹. Dark regions correspond to a director orientation in the xz - or yz -plane.

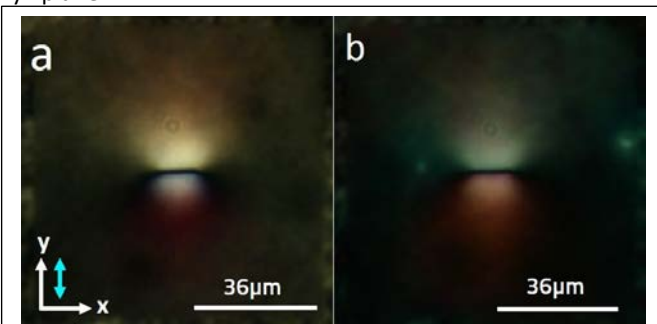


Fig. 2 Polarizing optical microscope image of opposite-sign defect cell for a) $E = 0 \text{ V m}^{-1}$ and b) $E = 8 \text{ V } \mu\text{m}^{-1}$. The double-headed arrow shows the polarizer orientation along the y -axis, with the analyser oriented along the x -axis.

Lavrentovich has written an excellent review of confocal fluorescence microscopy in LCs³⁸. Here the cell was placed in a Leica 2500M confocal fluorescence microscope, with excitation at wavelength 488 nm and polarization along the y -axis. For a fixed value of z , the optics facilitate imaging of the sample (with a vertical range $\delta z = \pm 1 \mu\text{m}$). The BTBP dye's average transition dipole moment aligns with the nematic director in low concentrations^{38,40}, causing it to fluoresce preferentially when the polarization of the exciting photon is parallel to the local nematic director. The intensity, in principle, vanishes when the director (and therefore the dye) is in the xz -plane. The actual intensity in the absence of a crossed polarizer is proportional to $\cos^2\theta$, where θ is the angle between the BTBP dye's transition dipole (approximately parallel to the LC director) and the laser polarization, which in our case is along the y -axis. This allows us

to reconstruct the nematic director in 3D with micron-scale resolution in the z -direction. We remark that an $m = +1$ surface defect presents two dark brushes in fluorescence confocal microscopy, but four brushes in POM. All measurements were performed at room temperature. Images were recorded at 0.5 μm increments along the z -axis from one substrate to the other. At each position along the z -axis a voltage V (frequency $f = 1000 \text{ Hz}$) was applied along this axis. The voltage was increased stepwise, with values of 0, 1.5, 3, 9, 18, 36, 57, 137, and 197 V,

after which the fluorescence imaging position was increased by $0.5 \mu\text{m}$ and another voltage set was collected.

3 Experimental Results and Discussion

a. Overview of Figures

Figure 2 shows POM images with crossed polarizers for the opposite-sign defect pairs. Figures 3 and 4 show confocal fluorescence images for the opposite-sign defect pairs, each at various positions above the patterned surface and at voltages corresponding to electric fields of 0, 0.37, 2.32 and $8.45 \text{ V } \mu\text{m}^{-1}$. Figure 5 shows POM images with crossed polarizers for the like-sign defect pairs, and Figs. 6 and 7 show fluorescence results. Here thickness $h = 25.0 \mu\text{m}$ for the opposite-sign defect pair (Figs. 2-4) and $24.5 \mu\text{m}$ for the same-sign pair (Figs. 5-7). (The small thickness difference is the reason for the electric field differences at the same applied voltages.)

b. Opposite-sign defect pair results and discussion

Figure 2 shows polarizing optical microscope images of the transmitted light through the entire cell for the opposite-sign defect pairs. Note that there is little change in the appearance

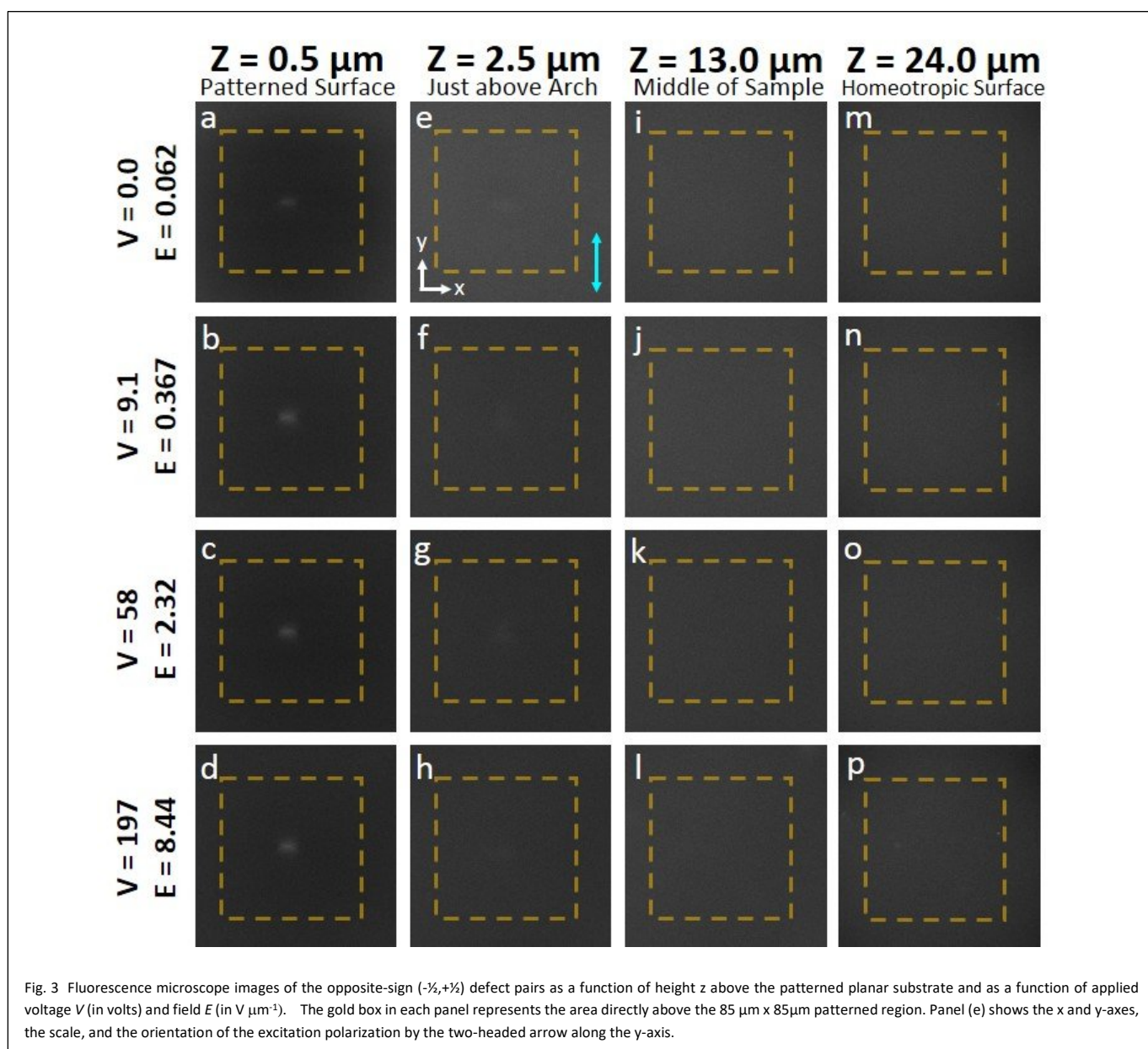


Fig. 3 Fluorescence microscope images of the opposite-sign ($-\frac{1}{2}, +\frac{1}{2}$) defect pairs as a function of height z above the patterned planar substrate and as a function of applied voltage V (in volts) and field E (in $\text{V } \mu\text{m}^{-1}$). The gold box in each panel represents the area directly above the $85 \mu\text{m} \times 85 \mu\text{m}$ patterned region. Panel (e) shows the x and y -axes, the scale, and the orientation of the excitation polarization by the two-headed arrow along the y -axis.

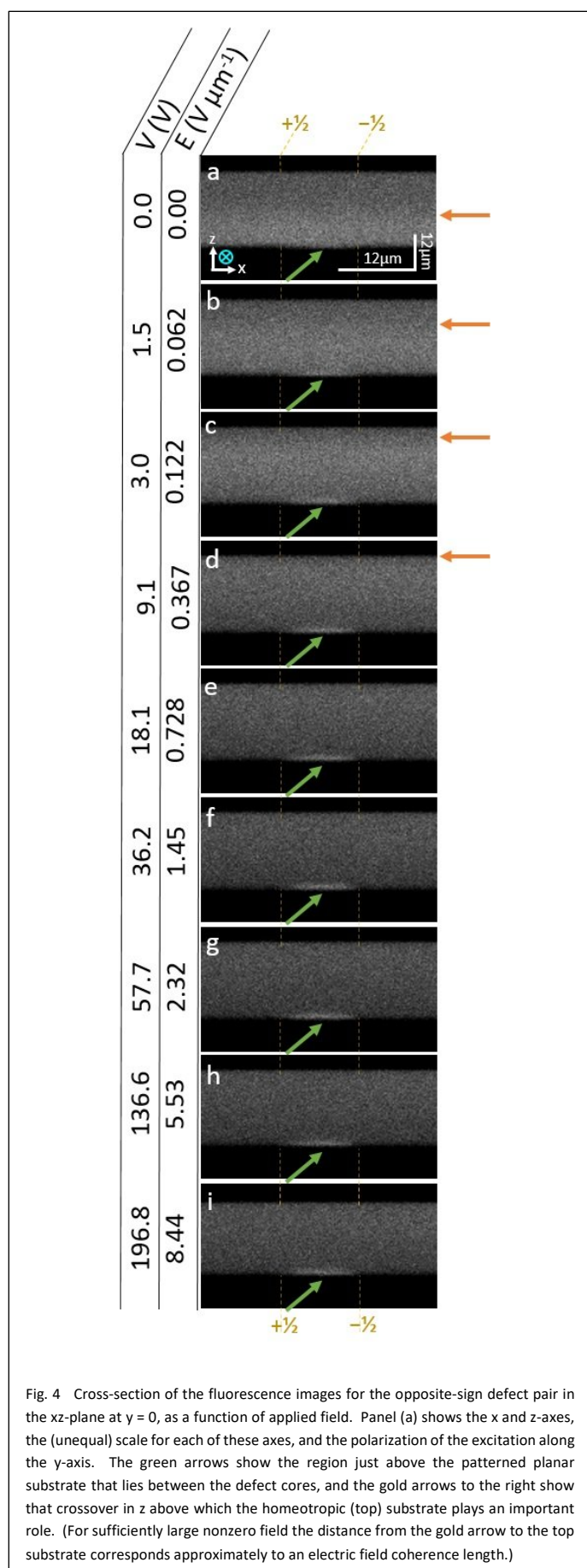


Fig. 4 Cross-section of the fluorescence images for the opposite-sign defect pair in the xz -plane at $y = 0$, as a function of applied field. Panel (a) shows the x and z -axes, the (unequal) scale for each of these axes, and the polarization of the excitation along the y -axis. The green arrows show the region just above the patterned planar substrate that lies between the defect cores, and the gold arrows to the right show that crossover in z above which the homeotropic (top) substrate plays an important role. (For sufficiently large nonzero field the distance from the gold arrow to the top substrate corresponds approximately to an electric field coherence length.)

of the disclination line connecting the defect cores as the electric field is increased.

Let us now turn to the fluorescence confocal imaging, with the excitation polarization along the y -axis. For the opposite-sign defects at $z = 0.5 \mu\text{m}$ near the patterned substrate and at fields $E = 0$ (Fig. 3a), 0.367 (Fig. 3b), 2.32 (Fig. 3c), and 8.45 (Fig. 3d) $\text{V } \mu\text{m}^{-1}$, one observes a slightly elongated bright region corresponding to the director (and therefore the dye) having an orientation along the y -axis in the region around and between the $m = \pm\frac{1}{2}$ defect pair and, importantly, *beneath the disclination arch*. There was only a slight increase in the fluorescence as the applied field was increased, as the field tended to suppress any out-of-plane component of the director. It is important to note that the total topological strength is zero, so that far from the defects the director becomes uniform along the x -axis. Thus, far from the defect cores, the fluorescence is very small.

The images in Figs. 3e through 3h correspond to the same voltages as for 3a-3d, respectively, but at $z = 2.5 \mu\text{m}$, just above the disclination arch. Here the director tends to have a strong in-plane component along the x -axis, which reduces the fluorescence from that beneath the arch. In the middle of the cell at $z = 13.0 \mu\text{m}$ (Figs. 3i-l), and near the top (nominally homeotropic) substrate at $z = 24.0 \mu\text{m}$ (Figs. 3m-p), little fluorescence is observed: The field causes the director to lie mostly in the xz -plane, especially along the x -axis over most of this region, but along the z -axis within a small electric coherence length $\xi_E = (K/\epsilon_0 \Delta\epsilon)^{1/2}/E$ of the top surface. Here K is an elastic constant. In neither case (the director along the x - or z -axis) is significant fluorescence observed, which would have occurred only if there were a director component along the y -axis.

Figure 4 shows a cross-section of the fluorescence image in the xz -plane at $y = 0$, i.e., through the axis connecting the two defects in each pair, as a function of applied field. (Note the difference in scales between the x and z -axes.) Here the laser polarization is again along the y -axis, into the page. The green arrow shows a bright stripe of approximately $12 \mu\text{m}$ along the x -axis and of thickness approximately $2 \mu\text{m}$ along the z -axis. This corresponds to the region beneath the disclination arch, where the director tends to point mostly along the y -direction (Fig. 1a), and hence the dye fluoresces. Notice that the form of this bright region changes little once the electric field is greater than the small field that is sufficient to extinguish the z -component of the director. From Fig. 4 it is clear that the electric field plays little role in reorienting the director below the disclination arch. The gold arrow in each frame shows the position of a boundary between a less dark region at smaller z and more dark region closer to the homeotropic substrate. As one transits from the disclination arch to larger z the director undergoes a rotation consistent with a hybrid-aligned cell, so that the director becomes vertically aligned at the top of each image. This results in a transition from a dark band to an even darker band. That this transition can be discerned is because the microscope tends to show slightly more fluorescence for a director along the x -axis than along the z -axis – this is an instrumental artefact –

although both are much weaker than that for an orientation along the y -axis. This results in a slightly darker image when the director is aligned along the z -axis. The region at which the transition takes place moves to larger z with increasing field, with the darker region corresponding approximately to an electric coherence length ξ_E from the homeotropic surface when the electric field dominates; the approximate boundary of this region, is shown by the gold arrows

c. Like-sign defect results and discussion

Let us turn to the same-sign defect pair ($+\frac{1}{2}$, $+\frac{1}{2}$) in Figs. 5, 6, 7, and 8. Figure 5 shows POM images of the cell containing the same-sign defect pairs, again at $E = 0$ and $E = 8.45 \text{ V } \mu\text{m}^{-1}$. At zero field, the defects and disclination line are localized near the planar surface of the cell, thus the texture appears as an isolated bulk $m = +1$ defect containing four brushes. At the higher voltage, the disclination arch has decomposed into a pair

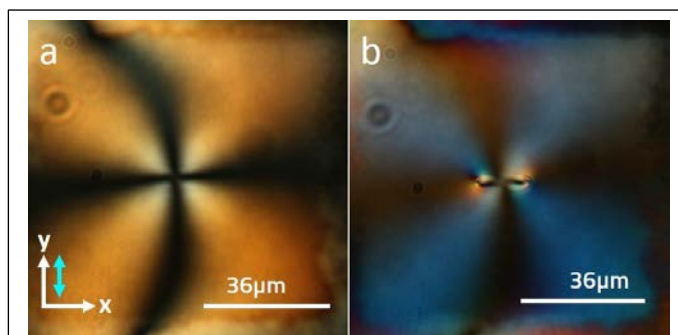


Fig. 5 POM microscope image of same-sign defect cell for a) $E = 0 \text{ V m}^{-1}$ and b) $E = 8 \text{ V } \mu\text{m}^{-1}$. The double-headed arrow shows the polarizer orientation.

of disclination lines traversing the sample. Note that four POM brushes remain present outside the disclination line region.

The layout of the same-sign defect pair fluorescence images in Fig. 6 is similar to Fig. 3, showing the fluorescence images at

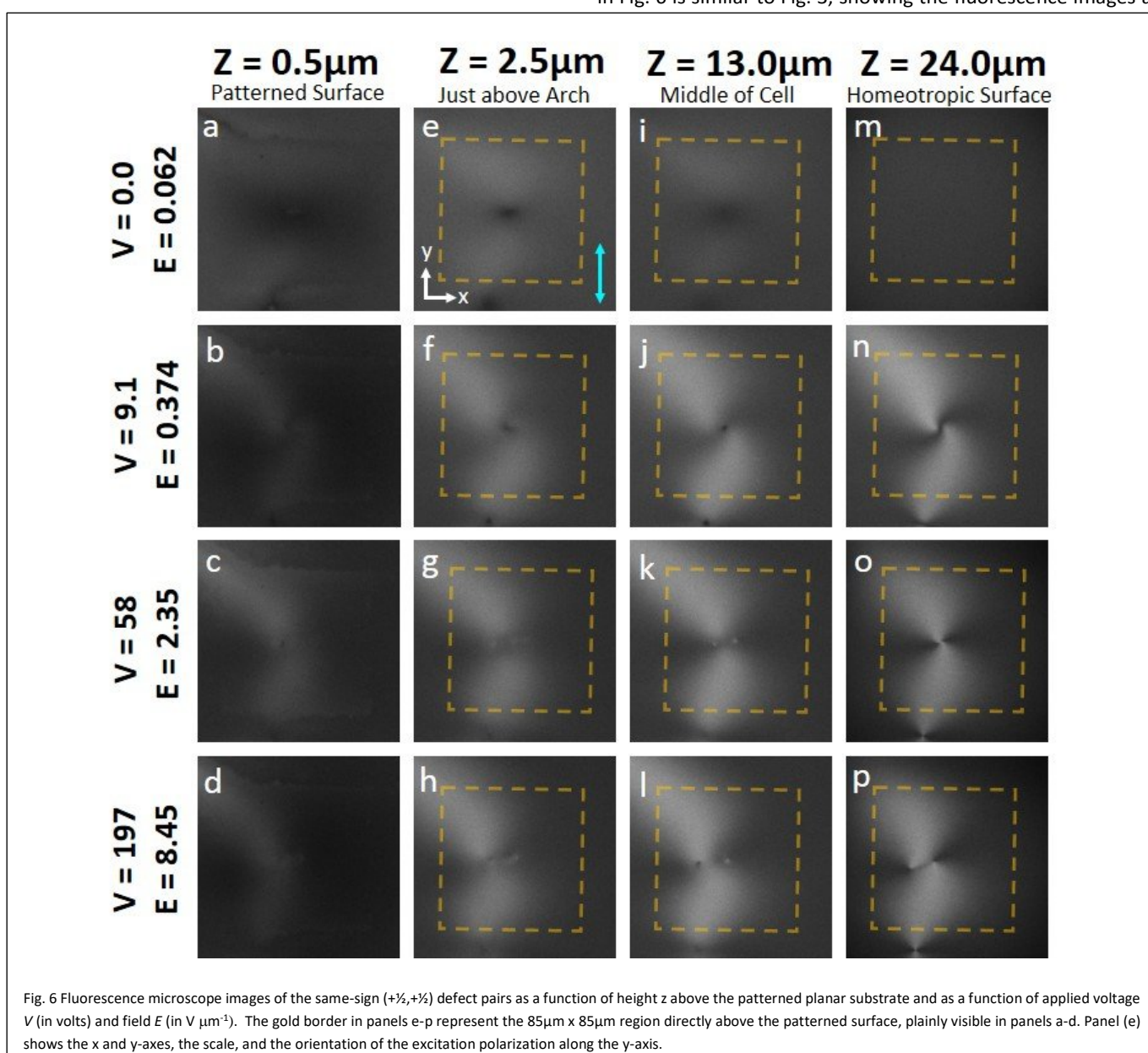


Fig. 6 Fluorescence microscope images of the same-sign ($+\frac{1}{2}$, $+\frac{1}{2}$) defect pairs as a function of height z above the patterned planar substrate and as a function of applied voltage V (in volts) and field E (in $\text{V } \mu\text{m}^{-1}$). The gold border in panels e-p represent the $85 \mu\text{m} \times 85 \mu\text{m}$ region directly above the patterned surface, plainly visible in panels a-d. Panel (e) shows the x and y -axes, the scale, and the orientation of the excitation polarization along the y -axis.

the same z values ($z = 0.5, 2.5, 13.0,$ and $24.0 \mu\text{m}$) with approximately the same applied fields of $E = 0, 0.37, 2.35,$ and $8.45 \text{ V } \mu\text{m}^{-1}$. Near the patterned substrate at $z = 0.5 \mu\text{m}$ (beneath the disclination arch) and with zero field applied, the fluorescent image (Fig. 6a) shows behaviour near the defects similar to Fig. 3a, *i.e.*, a slightly brighter band within a dark region. But far from the defect cores there is significant fluorescence. This occurs because the total topological strength $m = +1$, so that the director is radial far from the defects, and therefore lies mostly along the y -axis along the top and bottom of panel 6a. Hence, there is significant fluorescence in these regions. With increasing field (Figs. 6b-d) the results are qualitatively similar to those of Fig. 6a. Now moving to position $z = 2.5 \mu\text{m}$, which is just above position of the ground state (*i.e.*, $E = 0$) arch, we begin to see the effects of the field. As the field is increased, the dark spot observable in Fig. 6e, which corresponds to vertical alignment just above the arch's apex, evolves into two distinct spots, indicating that the arch is elongating and its apex is moving toward the homeotropic surface. Moreover, at the highest fields (Figs. 6g,h), one can begin to discern that the two spots, corresponding to the two legs of the disclination arch, are co-rotated slightly counter-clockwise⁴¹, which we believe is an artefact of the boundary conditions imposed by the two substrates, including the region outside the patterned square. These behaviours become even more evident in the middle of the sample, at $z = 13.0 \mu\text{m}$. Here we still see only a single diffuse spot at $E = 0$ (Fig. 6i), but which tightens on application of an electric field $E = 0.37 \text{ V m}^{-1}$ (Fig. 6j). This corresponds to homeotropic alignment above the arch's apex at this field. As the field is increased, the arch rises and the two legs of the disclination line become visible as two spots at higher fields (Figs. 6k,l). Finally, just beneath the homeotropic substrate, the image is uniformly dark at $E = 0$ (Fig. 6m), as the alignment is homeotropic throughout the slice. As the field is increased, the swirl pattern (Fig. 6n) becomes more pronounced, and indicates that the director projection in the xy -plane exhibits an $m = +1$ like defect with an apparently nonzero phase^{41,42}. Moreover, before attaining $E = 2.35 \text{ V m}^{-1}$, the arch's apex has reached the homeotropic surface and the disclination lines appear as two slightly separated spots (Fig. 6o). The disclination lines, and thus the spots, separate significantly at the homeotropically-treated substrate (Fig. 6p). The dark line connecting the half-integer defects in Fig. 6p corresponds to a wall separating reverse tilt domains⁴³⁻⁴⁵. This wall is a remnant of the homeotropic alignment imposed by the top substrate and the suppression of the director's z -component by the electric field on either side of the wall: The director lies along the z -axis on this wall, with reverse tilt domains on either side.

Let us now turn to Fig. 7, which is analogous to Fig. 4 but for the same-sign defect pair. At low fields we observe a diffuse dark region a few micrometers above the patterned substrate. This corresponds to a region that has strong vertical alignment. In fact, Fig. 8 shows the same slice as Fig. 7a, but with significant contrast enhancement and with x and z -axes having the same scale. Here the arch is clearly seen near the bottom, close to the patterned substrate. Above is a diffuse dark region, indicating strong alignment in the xz -plane. We see that the arch's apex at

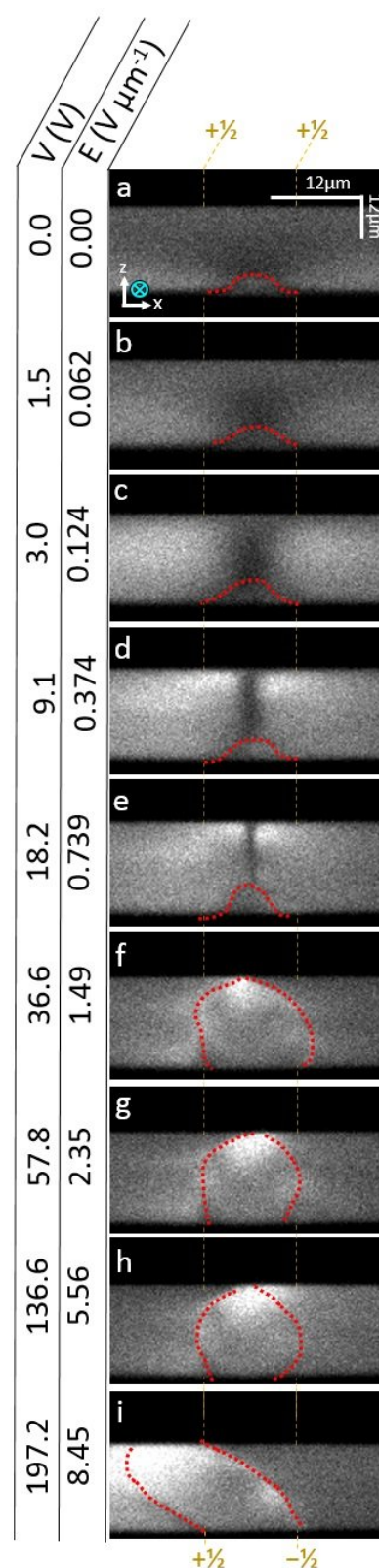


Fig. 7 Cross-section of the fluorescence images for the same-sign defect pair in the xz -plane at $y = 0$, as a function of applied field. Panel (a) shows the x and z -axes, the (unequal) scale for each of these axes, and the polarization of the excitation along the y -axis. The dotted red curves show the approximate position of the disclination arch.

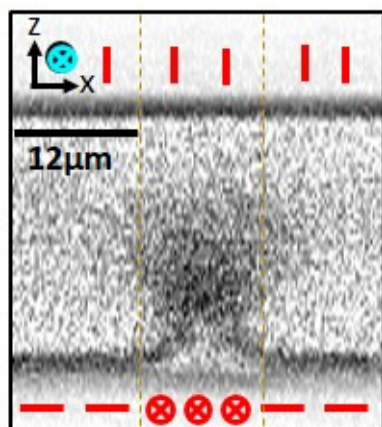


Fig. 8 The same as Fig. 7a but with enhanced contrast and an equal scale for the x and z-axes. The red lines and circled crosses represent the director orientation just inside the liquid crystal near the top (homeotropic) and bottom (patterned) substrates. Polarization direction is shown by the blue encircled X in the upper left.

$E = 0$ is considerably higher for the same-sign defect pair (Figs. 1b, 7a, and 8) than for the opposite-sign pair (see Figs. 1a and 4a). We believe that this is due to the 3D nature of the director field of the same-sign defect pair, which is repelled from the planar substrate as compared to the 2D director field of the opposite-sign defect pair. Returning to Fig. 7, in each image we have added a dotted red line indicating the approximate projection of the disclination line(s) into the xz -plane at $y = 0$. As mentioned above, the disclination line(s) may move out of the $y = 0$ plane (*cf.* Fig. 6n). As the field is increased, this diffuse dark region becomes more narrow, as seen in Figs. 7c–e. This is because the director is rotated (due to the field) toward the x -axis on either side of the arch's peak. This slightly weaker intensity near the top of each image to the far left and right of the central defect(s) is quantitatively consistent with, and can be seen in, Fig. 4a–e, where the regions below the gold arrow (director along the x -axis) are approximately 15% brighter than above the arrow (director along the z -axis). However, in Fig. 7c,d the image on either side, *but close to*, the arch's apex, tends to become brighter. This likely is due to a twisting of the arch, which already can be seen in Figs. 6f, 6j, and 6n at a field of $0.37 \text{ V } \mu\text{m}^{-1}$. Here the director no longer lies in the xz -plane in the probed slice, and therefore a brighter fluorescence can be observed. In Fig. 7f the disclination arch is approaching the homeotropically-patterned substrate, and in Figs. 7g–l the electric field correlation length has become sufficiently small that the (rotated) in-plane component of the director around the disclination lines is visible as bright regions throughout.

4 Numerical Simulations

To validate qualitatively the experimental results, we performed numerical simulations for the like-sign defect pair using an approximate treatment of the field, similar to the

method described in Ref. 16. For these calculations we use the Frank elastic constants appropriate for the liquid crystal ZLI-2806: $K_{11} = 14.9 \text{ pN}$, $K_{22} = 7.9 \text{ pN}$, $K_{33} = 15.4 \text{ pN}$ [Ref. 36]. For K_{24} we chose 14.8 pN based on the multiplicative relationship between K_{24} and K_{11} [Ref. 46], and the dielectric anisotropy $\Delta\epsilon = -4.8$ [Ref. 36]. We assume rigid anchoring conditions at both the patterned planar and the opposing homeotropic substrates.

Figure 9 shows the simulated director pattern around the disclination arch as a function of applied electric field for the same-sign ($+\frac{1}{2}, +\frac{1}{2}$) defect pair at the patterned planar substrate. As is apparent, the arch extends along the z -axis with increasing field, as the director orientation is compressed into the xy -plane, except close to the apex. This is especially visible in Fig. 9c, which represents the behaviour at a field just below the critical field at which the apex makes contact with the opposing substrate and the arch splits into two separate disclination lines that terminate at the two surfaces. The calculated field at which splitting occurs is slightly larger than $5 \text{ V } \mu\text{m}^{-1}$, which is larger than, but of the same order as, the experimental value of $E > 2.5 \text{ V } \mu\text{m}^{-1}$ (Fig. 7g,h). The discrepancy may be explained by limitations of the simulation approach: 1) infinitely strong anchoring conditions at the homeotropic substrate, 2) approximate treatment of the field, and 3) numerical pinning of the disclination line between lattice sites of the simulation. (Owing to the multiple factors enumerated above, it is difficult to attribute which of these factors contributes most to the discrepancy.) We note that (1), *viz.*, infinitely strong anchoring used in the simulations, has the effect of suppressing the rise of the disclination arch because the director around the arch tends to lie in the xy -plane. On the other hand, the finite anchoring strength in the experiment facilitates director tilt into the xy -plane, and therefore lowers the critical field, as observed. Despite the quantitative difference in critical field, both experiment and simulations show little, if any, change in the same-sign disclination with electric field, but both show a rising arch that reaches the opposing substrate at a critical field for the opposite-sign disclination.

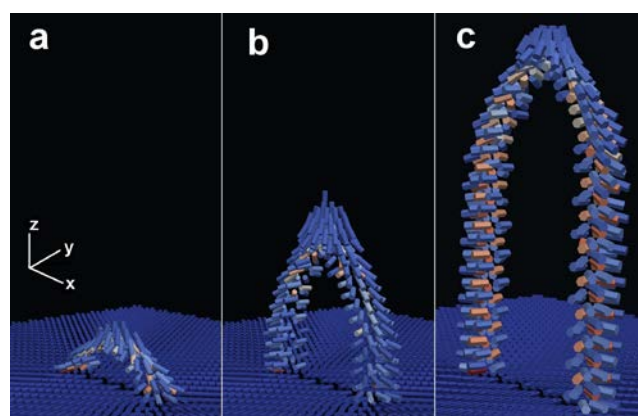


Fig. 9 Simulation of director pattern and disclination arch for a) $E = 0$, b) $E = 3.5$, c) $E = 5 \text{ V } \mu\text{m}^{-1}$

Another feature to note, most visible in Fig. 9b, is that the director pattern at the substrate and far from the surface disclinations is nearly radial, consistent with a pair of $m = +\frac{1}{2}$ defects. This orientation profile, which contains a strong y-axis component of the director, is the reason that Fig. 6a (and other panels in Fig. 6) show fluorescence far from the defect core region. However, unlike the experimental results shown in Fig. 6, the modelling shows no twisting of the disclination lines, neither with increasing field nor with position z inside the cell. As noted previously, we believe that the apparent experimental twist is due to a combination of surface imperfections and interactions with the randomly aligned region outside the scribed pattern.

5 Conclusions

First suggested by numerical calculations, we have shown experimentally that the disclination line connecting a pair of same-sign defects at a substrate is surrounded by a 3D director field. This director field can be driven into a quasi-2D plane, forcing a distortion of the disclination arch, and eventually breaking the arch into two disclination lines connecting the two substrates. On the other hand, the director field surrounding a disclination line that connects opposite-sign defects at the same surface is two-dimensional, and thus the electric field has no significant effect for a $\Delta\epsilon < 0$ liquid crystal. Thus, the results show that disclinations having a 3D director field can connect any pairing of surface defects of strength $m = +\frac{1}{2}$ or $-\frac{1}{2}$, as these disclinations can be transformed topologically from one into another. But this is not true of a 2D director field, which can be associated with distinct, topologically inequivalent disclinations that cannot transform continuously. Thus, not all half-integer surface defect pairs can be connected via a disclination line with a 2D director field. It is for this reason that the 3D disclination line, *i.e.*, the arch, connecting the pair of $m = +\frac{1}{2}$ same-sign surface defects is expelled when the director field is forced to become quasi 2D on application of a sufficiently strong electric field.

Conflicts of interest

There are no conflicts to declare.

Acknowledgements

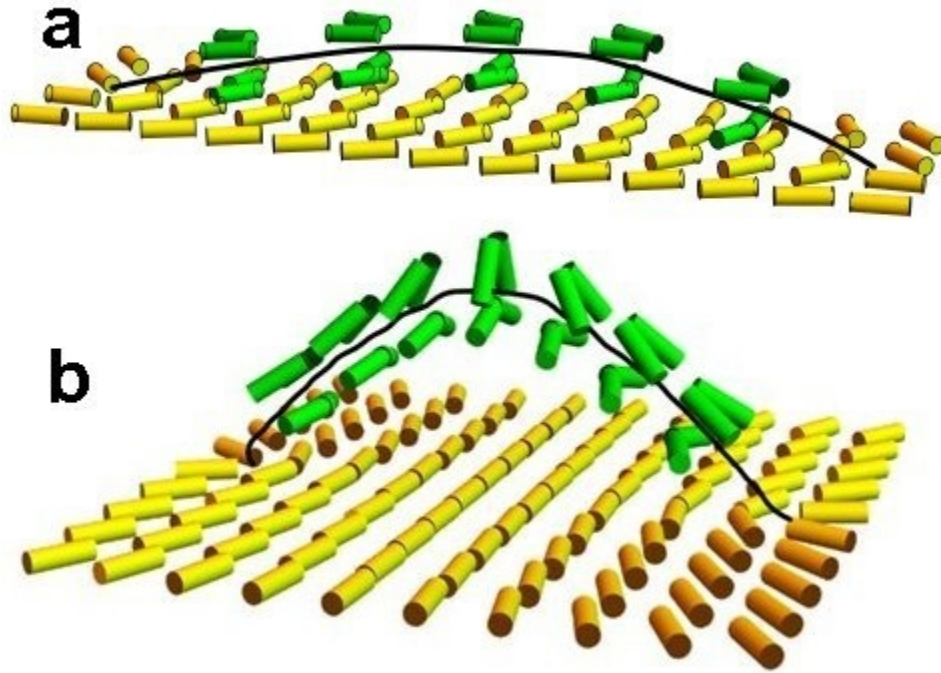
We thank Prof. Samo Kralj and Dr. Bryce Murray for useful conversations. This work was supported by the National Science Foundation under grants DMR1505389 and DMR1901797 (CWRU) and DMR1409658 (KSU), and the National Aeronautics and Space Administration under grant NNX17AC76G (CWRU).

Notes and references

- 1 N. Mermin, *Rev. Mod. Phys.*, 1979, **51**, 591.
- 2 W. H. Zurek, *Nature* 1985, **317**, 505

- 3 Y. Zhenwei and M.O. Cruz, *Proc. Nat. Acad. Sci.*, 2014, **111**, 5049
- 4 T.W.B. Kibble, *J. Phys. A Math Gen.*, 1976, **9**, 1387
- 5 A. Martinez, M. Ravnik, B. Lucerno, R. Visvanathan, S. Žumer, and I.I. Smalyukh, *Nature Mater.*, 2014, **13**, 258
- 6 M. Kleman and O.D. Lavrentovich, **Soft Matter Physics**, Springer-Verlag, New York 2003
- 7 F. Serra, *Liq. Cryst.*, 2016, **43**, 1920
- 8 S. Zhou, S.V. Shiyankovskii, H.-S. Park, and O.D. Lavrentovich, *Nature Comm.*, 2017, **8**, 14974 (DOI: 10.1038/ncomms14974)
- 9 D. Coursault, B. Zappone, A. Coati, A. Boulaoued, L. Pelliser, D. Limagne, N. Boudet, B.H. Ibrahim, A. DeMartino, M. Alba, M. Goldmann, Y. Garreau, B. Gallas, and E. Lacaze, *Soft Matter*, 2016, **12**, 678
- 10 I.R. Nemitz, I. Gryn, N. Boudet, R.P. Lemieux, M. Goldmann, B. Zappone, R.G. Petschek, C. Rosenblatt, and E. Lacaze, *Soft Matter*, 2018, **14**, 460
- 11 T.C. Lubensky and S.R. Renn, *Phys. Rev. A*, 1988, **38**, 2132
- 12 J.W. Goodby, M.A. Waugh, S.M. Stein, E. Chin, R. Pindak, and J.S. Patel, *Nature*, 1989, **337**, 449
- 13 C.S. Rosenblatt, R. Pindak, N.A. Clark, and R.B. Meyer, *J. Phys. (Paris)* 1977, **38**, 1105
- 14 A. S. Backer, A. C. Callan-Jones, and R. A. Pelcovits, *Phys. Rev. E* 2008, **77**, 021701
- 15 B.S. Murray, R.A. Pelcovits, and C. Rosenblatt, *Phys. Rev. E* 2014, **90**, 052501 (2014)
- 16 S. Afghah, R.L.B. Selinger, and J.V. Selinger, *Liq. Cryst.*, 2018, **45**, 2022
- 17 N.D. Mermin, *Rev. Mod. Phys.* 1979, **51**, 591
- 18 J.N. Eakin, Y. Xie, R.A. Pelcovits, M.D. Radcliffe, and G.P. Crawford, *Appl. Phys. Lett.*, 2004, **85**, 1671
- 19 G.P. Crawford, J.N. Eakins, M.D. Radcliffe, A. Callan-Jones, and R.A. Pelcovits, *J. Appl. Phys.* 2005, **98**, 123102
- 20 Z. Zhuang, S.-W. Suh, Y.J. Kim, and J.S. Patel, *Appl. Phys. Lett.*, 2000, **76**, 3005
- 21 Y. Yoshida, K. Asakura, J. Fukuda, and M. Ozaki, *Nature Comm.*, 2015, **6**, 7180
- 22 J.-B. Fleury, D. Pires, and Y. Galerne, *Phys. Rev. Lett.*, 1009, **103**, 267801
- 23 P.J. Ackerman, Z. Qi, and I.I. Smalyukh, *Phys. Rev. E* 2012, **86**, 021703
- 24 Y.B. Guo, M. Jiang, C.H. Peng, K. Sun, O. Yaroshchuk, O.D. Lavrentovich, and Q.H. Wei, *Adv. Mater.* 2016, **28**, 2353
- 25 K. Kawaguchi, R. Kageyama, and M. Sano, *Nature*, 2017, **545**, 327
- 26 A. Martinez, M. Ravnik, B. Lucero, R. Visvanathan, S. Žumer, and I.I. Smalyukh, *Nature Mater.*, 2014, **13**, 259
- 27 B. Senyuk, Q. Liu, Y. Yuan, and I.I. Smalyukh, *Phys. Rev. E*, 2016, **93**, 062704
- 28 I.I. Smalyukh, *Liquid Crystal Colloids* in Annual Review of Condensed Matter Physics, Vol. 9, ed by S. Sachdev and M.C. Marchetti, 2018, p. 207
- 29 M. Nikkhou, M. Skarabot, and I. Musevic, *Phys. Rev. E*, 2016, **93**, 062703
- 30 M. Nikkhou and I. Musevic, *Soft Matter*, 2018, **14**, 9819
- 31 M. Nikkhou, H.F. Gleeson, and I. Musevic, *Liquid Cryst.*, 2018, **45**, 2294
- 32 M.S. Kim and F. Serra, *RSC Adv.*, 2018, **8**, 35640
- 33 S.J. DeCamp, G.S. Redner, A. Baskaran, M.F. Hagan, and Z. Dogic, *Nature Mater.*, 2015, **14**, 1110
- 34 G. Duclos, R. Adkins, D. Banerjee, M.S.E. Peterson, M. Varghese, I. Kolvin, A. Baskaran, R.A. Pelcovits, T.R. Powers, A. Baskaran, F. Toschi, M.F. Hagan, S.J. Streichan, V. Vitelli, D.A. Beller, and Z. Dogic, arXiv:1909.01381 [cond-mat.soft]

- 35 B.S. Murray, S. Kralj, and C. Rosenblatt, *Soft Matter*, 2017, **13**, 8442
- 36 L.C. Chien, T. Doi, and K. Mie, U.S. Patent 7,090,901 (2006)
- 37 R.P. Trivedi, I.I. Klevets, B. Senyuk, T. Lee, and I.I. Smalyukh, *Proc. Nat. Acad. Sci.*, 2012, **109**, 4744
- 38 O.D. Lavrentovich, *Pramana*, 2003, **61**, 373
- 39 B. Wen, M.P. Mahajan, and C. Rosenblatt, *Appl. Phys. Lett.* 2000, **76**, 1240
- 40 I.I. Smalyukh, R. Pratibha, N.V. Madhusudana, and O.D. Lavrentovich, *Eur. Phys. J. E*, 2005, **16**, 179
- 41 X. Tang and J.V. Selinger, *Soft Matter*, 2017, **13**, 5481
- 42 J. Nehring and A. Saupe, *J. Chem. Soc. Faraday Trans 2*, 1972, **68**, 1
- 43 D.K. Shenoy, J.V. Selinger, K.A. Grüneberg, J. Naciri, and R. Shashidhar, *Phys. Rev. Lett.*, 1999, **82**, 1716
- 44 S.H. Lee, T.-H. Yoon, J.C. Kim, and G.-D. Lee, *J. Appl. Phys.*, 2006, **100**, 064902
- 45 R. Wang, T.J. Atherton, M. Zhu, R.G. Petschek, and C. Rosenblatt, *Phys. Rev. E*, 2007, **76**, 021702
- 46 A.A. Joshi, J.K. Whitmer, O. Guzman, N.L. Abbot and J.J. de Pablo, *Soft Matter*, 2014, **10**, 882



167x119mm (72 x 72 DPI)